Finite-difference quasi-P traveltimes for anisotropic media

Jianliang Qian

Formerly The Rice Inversion Project, Department of Computational and Applied Mathematics, Rice University, Houston, TX 77251-1892; presently Institute for Mathematics and Its Applications, University of Minnesota, 400 Lind Hall, 207 Church St. S.E., Minneapolis, MN 55455. email qian@ima.umn.edu

William W. Symes

The Rice Inversion Project, Department of Computational and Applied Mathematics, Rice University, Houston, TX 77251-1892. email symes@caam.rice.edu

ABSTRACT

The first-arrival quasi-P wave traveltime field in an anisotropic elastic solid solves a first-order nonlinear partial differential equation, the qP eikonal equation. The difficulty in solving this eikonal equation by a finite-difference method is that for anisotropic media the ray (group) velocity direction is not the same as the direction of traveltime gradient, so that the traveltime gradient can no longer serve as an indicator of the group velocity direction in extrapolating the traveltime field. However, establishing an explicit relation between the ray velocity vector and the phase velocity vector overcomes this difficulty. Furthermore, the solution of the **paraxial** qP eikonal equation, an evolution equation in depth, gives the first-arrival traveltime along downward propagating rays. A second-order upwind finite-difference scheme solves this paraxial eikonal equation in O(N) floating point operations, where N is

the number of grid points. Numerical experiments using 2-D and 3-D transversely isotropic models demonstrate the accuracy of the scheme.

INTRODUCTION

Traveltime computation plays a central role in many seismic data processing methods, such as Kirchhoff depth migration and tomographic velocity analysis. Since seismic wave propagation is anisotropic in many sedimentary rocks, maximal imaging resolution requires that traveltime computation honor anisotropy whenever it seriously affects data kinematics (Pratt and Chapman, 1992; Tsvankin and Thomsen, 1995; Anderson, 1996; Cherrett and Singh, 1998).

Contemporary traveltime computation methods fall roughly into two classes: ray tracing methods and finite-difference eikonal solvers. Ray tracing and related methods for isotropic propagation extend without essential difficulty to anisotropic propagation, but they suffer from shadow zones and related interpolation problems (Cerveny, 1972; Shearer and Chapman, 1988; Meng and Bleistein, 1997) which complicate robust implementations. Finite-difference eikonal solvers compute approximate first-arrival times directly on a prespecified grid (Reshef and Kosloff, 1986; Vidale, 1988; van Trier and Symes, 1991; Schneider et al., 1992; Qin and Schuster, 1993; Schneider, 1995; Sethian and Popovici, 1999; Kim and Cook, 1999), involve rather simple data structures, and are easy to code efficiently. Extension of these methods to anisotropic wave propagation is not entirely straightforward. The methods cited here and others in the public literature describe only finite-difference traveltime algorithms for isotropic media.

The finite-difference eikonal solvers cited above depend on the fact that for isotropic media the ray velocity vector, i.e. the *group velocity*, has the same direction as the traveltime gradient, i.e. the *phase velocity*, so that we can use the traveltime gradient as a reliable indicator of energy flow (and thus causality) in extrapolating

the traveltime field. However, this is no longer true for anisotropic media (Dellinger and Symes, 1997). The goal of the current paper is to establish a reliable indicator of qP ray velocity direction by formulating a relation between the group velocity direction and the phase velocity direction, and to present theoretical formulations, some implementation details, and illustrative applications of a finite-difference method for traveltimes of first-arriving quasi-compressional waves in heterogeneous anisotropic solids.

The mathematical foundation of the finite-difference approach to traveltime computation is the observation of Lions (1982): the first-arrival traveltime is a generalized solution of the eikonal equation. A generalized solution concept is necessary because the eikonal equation does not generally have differentiable solutions everywhere in the ordinary sense throughout its domain. However, generalized solutions are not unique because of the existence of several branches of traveltime in the presence of strong refraction. Lions and others abstractly characterized a particular generalized solution, which turns out to be the first arrival. Because of its stability with respect to the medium parameters, source location, etc., this generalized solution is computable by finite-difference approximation. This particular generalized solution is the so-called viscosity solution (Crandall and Lions, 1983); for a good review of this concept, see Crandall, Ishii and Lions (1992).

The result of Lions (1982) pertains to isotropic media. The central hypothesis of this paper is that the first-arrival quasi-compressional ("qP") traveltime is also a stable generalized solution, and therefore computable by suitable finite-difference schemes. Also by analogy with the isotropic case, we expect so-called upwind schemes to be particularly successful (van Trier and Symes, 1991). Dellinger and Symes (1991; 1997) investigated this possibility but did not give full details of a workable algorithm. This paper presents a family of algorithms of Essentially NonOscillatory ("ENO") type (Osher and Sethian, 1988; Osher and Shu, 1991), applied to a depth-evolution ("paraxial") form of the eikonal equation. The computed solution gives an accurate

approximate time at every point of a Cartesian grid, which is connected to the source by a first-arriving ray whose velocity vector makes an angle less than a prescribed angle with the vertical. A similar approach has proven quite successful for isotropic traveltime (and amplitude) computation for use in prestack modeling, migration, and inversion (Symes et al., 1994; El-Mageed et al., 1997; Qian et al., 1999). We expect similar applications for the algorithm presented here.

We first derive the eikonal equation for the qP wave, which is the fastest propagating body wave. [The kinematics of qP waves are considerably simpler than those of quasi-shear phases; an effective finite-difference approach to the latter awaits resolution of difficult technical issues.] For downgoing qP waves, the eikonal equation can be transformed to an evolution equation in depth, which we call the paraxial eikonal equation. Definition of the paraxial eikonal depends on the relation of the aperture limitation, i.e. the indicator of the energy flow, defined in terms of the ray velocity vector and the traveltime gradient. We show how to formulate this relation and mention the simplifications which occur in the presence of transverse isotropy with a vertical symmetry axis (VTI media). The VTI assumption permits us to give closed form expressions for all of the quantities appearing in the paraxial eikonal equation in terms of Thomsen's parameters (Thomsen, 1986), whereas in general these must be computed using numerical eigenvalue solvers. We use the ENO-Godunov family of finite-difference schemes (Osher and Sethian, 1988; Osher and Shu, 1991) to build qP eikonal solvers of arbitrary order of accuracy, in two- or three-dimensions. Two and three dimensional VTI examples illustrate the accuracy of the ENO schemes as well as the effect of the paraxial (aperture-limiting) assumption. Application to (isotropic and anisotropic) Marmousi models (Alkhalifah, 1997) shows the ability of these schemes to reveal the kinematic effect of anisotropy in geologically complex models.

THE PARAXIAL EIKONAL EQUATIONS FOR QP WAVES

In velocity structures with mild lateral heterogeneity, most reflected wave energy propagates down to the target, then up to the surface. That is, the energy in such a wavefield propagates along downgoing rays: the x_3 ("z") component of the ray velocity vector remains positive from source to target. The traveltime along such downgoing rays increases with depth and should be the solution of an evolution system in depth. For isotropic wave propagation, Gray and May (1994) suggested modifying the eikonal equation in such a way that (i) the modified equation defines a depth evolution of traveltime, and (ii) solutions of the modified and original eikonal equation are identical at every point connected to the source by a first-arriving ray making a angle with the vertical less than 90 degrees. The principal purpose of this section is to explain such a modification, resulting in a *paraxial eikonal equation*, for anisotropic propagation.

High frequency approximation to the elastic equation of motion leads to the Christoffel equation (Musgrave, 1970, p. 84),

$$\sum_k (\sum_{i,l} a_{ijkl} p_i p_l - \delta_{jk}) U_k = 0, \tag{1}$$

in which a_{ijkl} are the components of the elastic (Hooke) tensor divided by density, U_k is displacement vector for a particular asymptotic phase, $\mathbf{p} = \nabla\tau$ is the slowness vector, τ is the traveltime or phase of the mode, and δ_{jk} is the Kronecker delta. Note that all of these quantities depend on the spatial coordinate vector $\mathbf{x} = (x_1, x_2, x_3)$, though in this and some of the following displays this dependence has been suppressed for the sake of clarity. This equation has nontrivial solutions U_k only when

$$\det (\sum_{i,l} a_{ijkl} p_i p_l - \delta_{jk}) = 0. \tag{2}$$

The Christoffel matrix $\sum_{i,l} a_{ijkl} p_i p_l$ is positive definite and scales as $p^2 = \mathbf{p} \cdot \mathbf{p}$. Therefore each eigenvalue takes the form $v^2(\mathbf{x}, \mathbf{p}) p^2$, where v is a homogeneous function of degree zero in $\mathbf{p}$. The largest eigenvalue, denoted $v_{qP}^2(\mathbf{x}, \mathbf{p}) p^2$, is simple

(Fedorov, 1968, p. 95), hence depends smoothly on the components of the Christoffel matrix, i.e. on $\mathbf{p}$, and the Hooke tensor. The slowness vector $\mathbf{p}$ for which

$$S(\mathbf{x}, \mathbf{p}) \equiv |\mathbf{p}| v_{qP}(\mathbf{x}, \mathbf{p}) = 1, \tag{3}$$

forms the **qP slowness surface**, and v_{qP} is the qP phase velocity. Note that these slowness vectors solve the Christoffel equation (2).

The qP wave eikonal equation results from combining the slowness surface condition (3) with the slowness identity $\mathbf{p} = \nabla\tau$:

$$S(\mathbf{x}, \nabla\tau) = 1. \tag{4}$$

The method of characteristics relates its solution τ of slowness surface equation (4) to the rays of geometrical optics, which are the solutions of the ordinary differential equations

$$\frac{d\mathbf{x}}{dt} = \nabla_{\mathbf{p}} S(\mathbf{x}, \mathbf{p}), \tag{5}$$

$$\frac{d\mathbf{p}}{dt} = -\nabla_{\mathbf{x}} S(\mathbf{x}, \mathbf{p}), \tag{6}$$

where we have used the homogeneity of the eigenvalue v_{qP} in $\mathbf{p}$, so that $\tau = t$ has the dimension of time.

Downgoing rays correspond to the part of the slowness surface on which $\frac{dx_3}{dt} > 0$. A useful description of this part of the surface follows from its **convexity** (Musgrave, 1970, p. 92): the slowness surface defined by equation (2) is sextic and consists of three sheets corresponding to three different waves; if the inner detached slowness sheet related to quasi-P waves is not wholly strictly convex, a straight line could intersect the inner sheet at 4 or more points and yet make at least 4 further intersections with the remaining sheets; but any straight line must intersect the slowness surface at only 6 points, real or imaginary because the slowness surface is sextic. By Theorem A.1 in Qian (2000), we have that

- for each $\mathbf{x}$ and horizontal slowness vector (p_1, p_2), there are at most two choices of p_3 for which $\mathbf{p} = (p_1, p_2, p_3)$ solves the slowness surface equation (4);

- when two distinct solutions exist, by equation (5) only one satisfies (Figure 1)

$$\frac{dx_3}{dt} = \frac{\partial S(\mathbf{x}, \mathbf{p})}{\partial p_3} > 0.$$

This choice defines p_3 as a function of $\mathbf{x}, p_1, p_2$:

$$p_3 = H(\mathbf{x}, p_1, p_2), \tag{7}$$

which is also a partial differential equation for τ with H a concave Hamiltonian.

The characteristics (rays) of eikonal equation (7) are downgoing, so they can be parameterized by $x_3 = z$ and satisfy

$$\frac{dx_i}{dx_3} = -\frac{\partial H}{\partial p_i}, \ i = 1, 2; \tag{8}$$

$$\frac{d\tau}{dx_3} = H - p_1 \frac{\partial H}{\partial p_1} - p_2 \frac{\partial H}{\partial p_2}. \tag{9}$$

The ray group velocity is

$$v_g \ = \ \frac{\sqrt{\left(\frac{\partial H}{\partial p_1}\right)^2 + \left(\frac{\partial H}{\partial p_2}\right)^2 + 1}}{H(p_1, p_2) - \frac{\partial H}{\partial p_1} p_1 - \frac{\partial H}{\partial p_2} p_2}, \tag{10}$$

where

$$\frac{\partial H}{\partial p_1} \ = \ -\frac{a_{1jkl} p_l g_j g_k}{a_{3jkl} p_l g_j g_k}, \tag{11}$$

$$\frac{\partial H}{\partial p_2} \ = \ -\frac{a_{2jkl} p_l g_j g_k}{a_{3jkl} p_l g_j g_k}, \tag{12}$$

with g_j the eigenvector corresponding to v_{qP} and the Einstein summation convention assumed.

However neither the partial differential equation (7) nor its rays are well-defined for all p_1, p_2. To remedy this defect, we introduce another family of Hamiltonian functions

H_Δ, each of which is identical to H along "safely downgoing" rays, and defined everywhere in phase space. It is convenient to parametrize the horizontal variables (p_1, p_2) by polar coordinates: $(p_1, p_2) = (p' \cos\phi, p' \sin\phi)$, where $p' = \sqrt{p_1^2 + p_2^2}$. For each planar angle ϕ, the family of planes perpendicular to $(\cos\phi, \sin\phi, 0)$ is tangent to the slowness surface at exactly one point $(p'_{\max}(\phi)\cos\phi, p'_{\max}(\phi)\sin\phi, p_3(\phi))$ since the quasi-P slowness surface is strictly convex, where $p'_{\max}$ is the length of the horizontal slowness vector defined by that tangent point. Choose $0 < \Delta < 1$ and consider a given ϕ: for $p' \le (1-\Delta)p'_{\max}(\phi)$, set $H_\Delta(p'\cos\phi, p'\sin\phi) = H(p'\cos\phi, p'\sin\phi)$, which is the unique root of $S = 1$ with $p_3 > p_3(\phi)$; for $p' > (1-\Delta)p'_{\max}(\phi)$, set $H_\Delta(p'\cos\phi, p'\sin\phi) = H((1-\Delta)p'_{\max}(\phi)\cos\phi, (1-\Delta)p'_{\max}(\phi)\sin\phi)$. By construction, H_Δ remains concave by Theorem A.4 in Qian (2000); rays of H_Δ are rays of H, and hence of the anisotropic elastic model, so long as their horizontal slowness components $(p'\cos\phi, p'\sin\phi)$ satisfy $p' \le (1-\Delta)p'_{\max}(\phi)$.

By Corollary A.2 in Qian (2000), the ray angle ψ stays safely away from 90 degrees:

$$
\begin{aligned}
|\tan\psi| &= \frac{\sqrt{\left(\frac{\partial x_1}{\partial\tau}\right)^2 + \left(\frac{\partial x_2}{\partial\tau}\right)^2}}{\frac{\partial x_3}{\partial\tau}} \\
&= \sqrt{\left(\frac{\partial H_\Delta}{\partial p_1}\right)^2 + \left(\frac{\partial H_\Delta}{\partial p_2}\right)^2} \le O(\frac{1}{\Delta}).
\end{aligned} \tag{13}
$$

Numerical algorithms for the **paraxial eikonal equation**

$$
\frac{\partial\tau}{\partial x_3} = H_\Delta\left(\mathbf{x}, \frac{\partial\tau}{\partial x_1}, \frac{\partial\tau}{\partial x_2}\right), \tag{14}
$$

require explicit bounds on $\tan\psi$. Because of the convexity of the slowness surface, we need only look for these at the boundary of the region where $H_\Delta = H$, i.e. where $p' = (1-\Delta)p'_{\max}(\phi)$. Since H_Δ is radially constant outside of this region, the required bound is simply the maximum length of the 2-vector $\left(\frac{\partial H_\Delta}{\partial p_1}, \frac{\partial H_\Delta}{\partial p_2}\right)$ over the set $\{p' = (1-\Delta)p'_{\max}(\phi)\}$.

For the remainder of this paper, we put aside any further development of the algorithm for general anisotropy and pass to consideration of a special case, in which

most of the details of the paraxial Hamiltonian construction are much simpler. For the complete theoretical justification of the paraxial eikonal equation, please see Qian (2000).

APPLICATION: VTI MEDIA

The elastic modulus matrix for a transversely isotropic medium with a vertical symmetry axis(VTI) has five independent components among twelve nonzero components (Musgrave, 1970; Thomsen, 1986). A closed form solution exists in this case for the eigenvalue problem, equation (2). Consequently, the slowness surface for qP waves can be simplified to

$$\tilde{S}(p_1, p_2, p_3) \equiv p_3^2 - \frac{2c}{-b + \sqrt{b^2 - 4ac}} = 0, \tag{15}$$

where

$$a \equiv \alpha_0^2 \beta_0^2, \tag{16}$$

$$b \equiv 2\alpha_0^2 \beta_0^2 (1 + \delta + (\epsilon - \delta)\frac{\alpha_0^2}{\beta_0^2})(p_1^2 + p_2^2) - \alpha_0^2 - \beta_0^2, \tag{17}$$

$$c \equiv ((1 + 2\epsilon)\alpha_0^2 (p_1^2 + p_2^2) - 1)(\beta_0^2 (p_1^2 + p_2^2) - 1), \tag{18}$$

with Thomsen's parameters (Thomsen, 1986) (Anderson, 1996, p. 19): α_0 and β_0 are the vertical sound speeds for qP and qS waves, and ϵ and δ are two measures of anisotropy.

Note that $\tilde{S}$ is in a form different from S, but they are equivalent in the sense that they characterize the same qP slowness surface, therefore $\tilde{S}$ must be convex. Clearly,

$$\frac{\partial \tilde{S}}{\partial p_3} = 2p_3 > 0 \tag{19}$$

if

$$p_3 = \sqrt{\frac{2c}{-b + \sqrt{b^2 - 4ac}}} > 0, \tag{20}$$

where we have taken the positive square root of equation (15). This equation applies to all ϵ and δ values regardless of the weak anisotropy assumptions. Hence the qP eikonal equation for VTI is

$$p_3 = H(p_1, p_2) = \sqrt{\frac{2c}{-b + \sqrt{b^2 - 4ac}}}. \tag{21}$$

To obtain the paraxial Hamiltonian, we need consider only the case of radial angle $\phi = 0$ in the horizontal slowness space because of the rotational symmetry about the vertical axis. First note that for VTI media, we have

$$\sqrt{p_1^2 + p_2^2} = \frac{\sin\theta}{v_{qP}(\theta)}, \tag{22}$$

$$p_3 = \frac{\cos\theta}{v_{qP}(\theta)}, \tag{23}$$

where θ is the phase angle with the vertical direction and $v_{qP}(\theta)$ is the related qP phase velocity. Secondly, because the function $\dfrac{\partial \tilde{S}}{\partial p_3}$ is strictly monotonic, we only need to know where $\dfrac{\partial \tilde{S}}{\partial p_3} = 0$ so that we can find horizontal rays. It follows that p_3 has to be zero since $\dfrac{\partial \tilde{S}}{\partial p_3} = 2p_3$, so the corresponding phase angle $\theta = \dfrac{\pi}{2}$. Therefore,

$$p_{\max}^{'}(0) = \left(\sqrt{p_1^2 + p_2^2}\right)_{\max} = \frac{1}{v_{qP}(\frac{\pi}{2})}. \tag{24}$$

Thus

$$H_\Delta(p_1, p_2) = \begin{cases} H(p_1, p_2),\ p = \sqrt{p_1^2 + p_2^2} \le \dfrac{(1-\Delta)}{v_{qP}(\frac{\pi}{2})}; \\ H\left(\dfrac{(1-\Delta)\cos\phi}{v_{qP}(\frac{\pi}{2})}, \dfrac{(1-\Delta)\sin\phi}{v_{qP}(\frac{\pi}{2})}\right), \text{ else.} \end{cases} \tag{25}$$

Notice that when we set $\phi \equiv 0$ in the second branch statement, we will get a two-dimensional Hamiltonian for a 2-D VTI medium. Next we want to simplify the above Hamiltonian. For $0 < \Delta < 1$, if we apply the Intermediate Value Theorem to the function $f(\theta) = \dfrac{\sin\theta}{v_{qP}(\theta)}$ in interval $[0, \dfrac{\pi}{2}]$, there exists $0 < \theta_{\max} < \frac{\pi}{2}$ such that

$$\frac{\sin\theta_{\max}}{v_{qP}(\theta_{\max})} = \frac{(1-\Delta)}{v_{qP}(\frac{\pi}{2})}. \tag{26}$$

Substitute the above relation into paraxial Hamiltonian (25) and combine the two branch statements into one, and we have

$$H_{\theta_{\max}}(p_1, p_2) = \sqrt{\max\left(\frac{2c}{-b+\sqrt{b^2-4ac}}, \frac{\cos^2(\theta_{\max})}{v_{qP}^2(\theta_{\max})}\right)}, \tag{27}$$

where we have used the subscript $\theta_{\max}$ to emphasize the dependence of the Hamiltonian on phase angle $\theta_{\max}$. We call $\theta_{\max}$ the maximum phase angle. This Hamiltonian implies that we can set up a maximum phase angle to obtain a paraxial Hamiltonian in VTI.

Finally we have a paraxial eikonal equation for qP wave in VTI,

$$p_3 = H_{\theta_{\max}}(p_1, p_2) = \sqrt{\max\left(\frac{2c}{-b+\sqrt{b^2-4ac}}, \frac{\cos^2(\theta_{\max})}{v_{qP}^2(\theta_{\max})}\right)}. \tag{28}$$

The two derivatives needed in the numerical algorithms satisfy

$$\frac{\partial H}{\partial p_1} = -\frac{p_1(2\alpha_0^2(1+2\epsilon)\beta_0^2(p_1^2+p_2^2) + Ap_3^2 - \alpha_0^2(1+2\epsilon) - \beta_0^2)}{p_3(2\alpha_0^2\beta_0^2 p_3^2 + A(p_1^2+p_2^2) - \alpha_0^2 - \beta_0^2)}, \tag{29}$$

$$\frac{\partial H}{\partial p_2} = -\frac{p_2(2\alpha_0^2(1+2\epsilon)\beta_0^2(p_1^2+p_2^2) + Ap_3^2 - \alpha_0^2(1+2\epsilon) - \beta_0^2)}{p_3(2\alpha_0^2\beta_0^2 p_3^2 + A(p_1^2+p_2^2) - \alpha_0^2 - \beta_0^2)}, \tag{30}$$

with

$$A = 2\alpha_0^2(\alpha_0^2(\epsilon-\delta) + \beta_0^2(1+\delta)). \tag{31}$$

ENO SCHEMES FOR PARAXIAL EIKONAL EQUATIONS

Equation (14) is a nonlinear first-order PDE for traveltime τ. However traveltime is not unique: when the elastic parameters vary with position, in general many rays pass over at least some points in the subsurface. More than one traveltime may be assigned to each such point. One choice of unique traveltime for each subsurface point is the **least time** ("first-arrival time"). It turns out that this first-arrival time field is a **solution** of the eikonal equation (in a generalized sense). In fact it is the only

possible single-valued choice of traveltime field uniquely and stably determined by the data (source position and elastic parameters). These assertions were established some time ago (Lions, 1982) for isotropic eikonal equations with convex Hamiltonians, and we surmise that they apply as well to anisotropic problems with a convex slowness surface.

To compute the first-arrival traveltime field by a grid-based finite-difference scheme, we derived a first-order upwind scheme from ray tracing, rather than directly from the eikonal equation (Qian, 2000). Because our use of ray tracing in the derivation inherently honors causality, the resulting difference scheme is upwind, a term more or less synonymous with causality in this setting.

The first-order upwind scheme is hopelessly inefficient; moreover the traveltime field produced by it is so inaccurate as to prevent convergent computation of associated fields such as take-off angles, amplitudes, etc. So we use the first-order scheme as a building block to design high-order schemes. To increase the order of convergence, we employ higher-order Essentially NonOscillatory (ENO) refinements (Osher and Sethian, 1988; Osher and Shu, 1991; Shu, 1998).

ENO schemes belong to a family of upwind schemes, which are attractive for the three reasons: (1) stable schemes of arbitrarily high order of accuracy exist, permitting accurate solutions on coarse grids; (2) versions exist in any dimension – in particular, three-dimensional analogues are available; (3) ENO schemes are easy to program.

The principal feature of the ENO scheme is high-order interpolation with adaptive stencils which tries to avoid high gradient regions whenever possible. Specifically, we use a high-order ENO discretization in x_1, x_2 direction. Then in $x_3 = z$ direction we use a high-order Total Variation Diminishing (TVD) Runge-Kutta scheme to guarantee nonlinear stability and high-order accuracy of the whole scheme.

Given mesh sizes Δx_1, Δx_2 and Δx_3, we denote $\tau^n_{m,k}$ as the numerical approximation to the viscosity solution (Lions, 1982) $\tau(x_1^m, x_2^k, x_3^n)$ of equation (14) at the grid point (x_1^m, x_2^k, x_3^n). The backward $(-)$ and forward $(+)$ first-order difference quo-

tient approximations to the left and right derivatives of $\tau(x_1, x_2, x_3)$ at the location (x_1^m, x_2^k, x_3^n) with respect to x_1 and x_2 are defined as

$$D_{x_1}^{\pm}\tau_{m,k}^n = \pm\frac{\tau_{m\pm1,k}^n - \tau_{m,k}^n}{\Delta x_1}, D_{x_2}^{\pm}\tau_{m,k}^n = \pm\frac{\tau_{m,k\pm1}^n - \tau_{m,k}^n}{\Delta x_2}. \tag{32}$$

The second-order ENO refinements to $\dfrac{\partial\tau}{\partial x_1}$ (Osher and Sethian, 1988) are

$$D_{x_1}^{+,2}\tau = D_{x_1}^{+}\tau - \frac{1}{2}\Delta x_1 m(D_{x_1}^{+}D_{x_1}^{+}\tau, D_{x_1}^{-}D_{x_1}^{+}\tau), \tag{33}$$

$$D_{x_1}^{-,2}\tau = D_{x_1}^{-}\tau + \frac{1}{2}\Delta x_1 m(D_{x_1}^{-}D_{x_1}^{-}\tau, D_{x_1}^{-}D_{x_1}^{+}\tau) \tag{34}$$

with

$$m(x, y) = \min(\max(x, 0), \max(y, 0)) + \max(\min(x, 0), \min(y, 0)). \tag{35}$$

ENO refinements for $\dfrac{\partial\tau}{\partial x_2}$ are defined similarly.

So a second-order ENO Runge-Kutta scheme for equation(14) can be formulated as

$$\tau_{m,k}^{n+\frac{1}{2}} = \tau_{m,k}^n + \Delta x_3^{cfl}\widehat{H}_\Delta\left(D_{x_1}^{+,2}\tau_{m,k}^n, D_{x_1}^{-,2}\tau_{m,k}^n, D_{x_2}^{+,2}\tau_{m,k}^n, D_{x_2}^{-,2}\tau_{m,k}^n\right), \tag{36}$$

$$\tau_{m,k}^{n+1} = \frac{1}{2}\left(\tau_{m,k}^n + \tau_{m,k}^{n+\frac{1}{2}} + \Delta x_3^{cfl}\widehat{H}_\Delta\left(D_{x_1}^{+,2}\tau_{m,k}^{n+\frac{1}{2}}, D_{x_1}^{-,2}\tau_{m,k}^{n+\frac{1}{2}}, D_{x_2}^{+,2}\tau_{m,k}^{n+\frac{1}{2}}, D_{x_2}^{-,2}\tau_{m,k}^{n+\frac{1}{2}}\right)\right), \tag{37}$$

where the flux $\widehat{H}_\Delta$ is defined by (Osher and Shu, 1991)

$$\widehat{H}_\Delta(u^+, u^-, v^+, v^-) = \mathrm{ext}_{u\in I(u^-,u^+)}\mathrm{ext}_{v\in I(v^-,v^+)}H_\Delta(u, v); \tag{38}$$

the function $\mathrm{ext}_{u\in I(a,b)} = \max_{a\le u\le b}$ if $a \le b$, $\mathrm{ext}_{u\in I(a,b)} = \min_{b\le u\le a}$ else; $I(a, b) = [\min(a, b), \max(a, b)]$; $\Delta {x_3}^{cfl}$ is Courant-Friedrichs-Lewy ("CFL") step,

$$\Delta {x_3}^{cfl}\left(\max_{p_1,p_2}\sqrt{\left(\frac{\partial H_\Delta}{\partial p_1}\right)^2 + \left(\frac{\partial H_\Delta}{\partial p_2}\right)^2}\right) \le \frac{\Delta x_1\Delta x_2}{\sqrt{{\Delta x_1}^2 + {\Delta x_2}^2}}, \tag{39}$$

with the maximum taken over the relevant range of p_1 and p_2.

Because the Hamiltonian H_Δ is concave, the above flux function $\widehat{H}_\Delta$ is not difficult to compute as long as the "sonic point" (at which $\dfrac{\partial H_\Delta}{\partial p_1}$ or $\dfrac{\partial H_\Delta}{\partial p_2}$ changes sign) is

located. Furthermore, from (29) and (30) we know that for VTI media the sonic point is at $p_1 = 0$ or $p_2 = 0$. Thus a second-order ENO Runge-Kutta scheme for equation (28) can be formulated as

$$\tau_{m,k}^{n+\frac{1}{2}} = \tau_{m,k}^{n} + \Delta x_3^{cfl} H_{\theta_{\max}} \left((\widehat{\frac{\partial \tau}{\partial x_1}})_{m,k}^{n}, (\widehat{\frac{\partial \tau}{\partial x_2}})_{m,k}^{n} \right), \tag{40}$$

$$\tau_{m,k}^{n+1} = \frac{1}{2} \left(\tau_{m,k}^{n} + \tau_{m,k}^{n+\frac{1}{2}} + \Delta x_3^{cfl} H_{\theta_{\max}} \left((\widehat{\frac{\partial \tau}{\partial x_1}})_{m,k}^{n+\frac{1}{2}}, (\widehat{\frac{\partial \tau}{\partial x_2}})_{m,k}^{n+\frac{1}{2}} \right) \right), \tag{41}$$

where

$$(\widehat{\frac{\partial \tau}{\partial x_1}})_{m,k}^{n} = \text{maxmod}(\max(D_{x_1}^{-,2}\tau_m^n, 0), \min(D_{x_1}^{+,2}\tau_m^n, 0)), \tag{42}$$

$$(\widehat{\frac{\partial \tau}{\partial x_2}})_{m,k}^{n} = \text{maxmod}(\max(D_{x_2}^{-,2}\tau_m^n, 0), \min(D_{x_2}^{+,2}\tau_m^n, 0)), \tag{43}$$

with maxmod returning the larger value in modulus.

NUMERICAL EXAMPLES

To give some idea of the accuracy obtainable with the difference schemes outlined in the preceding section, we demonstrate the scheme on smooth VTI models and the (isotropic and anisotropic) Marmousi model; that is, we solve the paraxial eikonal equation (28) by using a second-order ENO scheme. All examples are assumed to be of constant density.

First we have to address the traveltime initialization. Due to the singularity of the traveltime field at the source which will lead to the contamination of global numerical accuracy, to initialize the traveltime we have to use some special techniques, such as the adaptive grid method (Qian et al., 1999) or the local uniform mesh refinement (Kim and Cook, 1999). However, here we assume a homogeneous layer near the source (for which it is supposed to be easy to assign an accurate traveltime) and start the finite difference scheme some distance away from the source; namely, we use a nonlinear iteration method to compute the group velocity and initialize directly the traveltime at every grid point on a surface away from the source. This initialization

technique, called the analytic method, is a simplified version of a general shooting method, which is detailed in Qian (2000), for traveltimes in anisotropic media.

2-D VTI

The first example occupies the rectangle $\{-0.5 \text{ km} \le x_1 \le 0.5 \text{ km}, 0 \le x_3 \le 1 \text{ km}\}$; the source is located at $x_1 = 0.0$ km, $x_3 = 0.0$ km. The four Thomsen's parameters of homogeneous Green River Shale are $\alpha_0 = 3.330$ km/s, $\beta_0 = 1.768$ km/s, $\epsilon = 0.195$, $\delta = -0.220$.

Because the absolute value of the parameter δ differs from that of ϵ only slightly, the near-vertical anisotropic response is dominated by δ (Thomsen, 1986), so we use this example to demonstrate not only the accuracy of the second-order scheme, but also the capability of the scheme in capturing the anisotropy of wave propagation. The initial data depth for the finite-difference scheme is at $x_3 = 0.24$ km. The maximum phase angle is taken as $\theta_{\max} = 80$ degrees. The results are shown on Table 1, where $\Delta x_3 = 0.01$ km, Abs.Err the maximum absolute error and Rel.Err the maximum relative error are both measured at bottom $x_3 = 1$ km. The formulae for the two errors are,

$$\text{Abs.Err}(\tau, \Delta x_1) = \max |\tau_{ana} - \tau_{fd}^{\Delta x_1}|,$$

$$\text{Rel.Err}(\tau, \Delta x_1) = \frac{\max |\tau_{ana} - \tau_{fd}^{\Delta x_1}|}{\max |\tau_{ana}|}$$

where τ_{ana} denotes the traveltime from the analytic method and τ_{fd} the traveltime from the finite difference scheme. Finally, α is the estimated convergence order,

$$\alpha = \frac{1}{\log 2} \log \left(\frac{\text{Rel.Err}(\tau, 2\Delta x_1)}{\text{Rel.Err}(\tau, \Delta x_1)} \right).$$

From this table, both the absolute error and relative error are decreased four times as Δx_1 is halved, and the accuracy order α is going to 2 as Δx_1 goes to zero, so this

scheme is of second-order accuracy. When $\Delta x_1 = \Delta x_3 = 0.01$ km, the maximum absolute traveltime error at bottom is less than $\frac{1}{50}$ ms.

In the second example, the model occupies the rectangle $\{-0.5 \text{ km} \le x_1 \le 0.5$ km, $0 \le x_3 \le 1$ km $\}$; the source is located at $x_1 = 0.0$ km, $x_3 = 0.0$ km. The four elastic parameters are

$$\begin{aligned}
\alpha_0 &= \sqrt{11.0889 + x_1 + x_3}, \\
\beta_0 &= \sqrt{3.1329 + 0.5x_1 + 0.5x_3}, \\
\epsilon &= \frac{4.3247 + x_1 + x_3}{2(11.0889 + x_1 + x_3)}, \\
\delta &= \frac{(4.9477 + x_1 + x_3)^2 - (7.9560 + 0.5x_1 + 0.5x_3)^2}{2(11.0889 + x_1 + x_3)(7.9560 + 0.5x_1 + 0.5x_3)},
\end{aligned}$$

which are perturbations to Thomsen's parameters of homogeneous Green River Shale. To simulate the VTI media, these parameters necessarily satisfy the stress-strain coefficient inequalities (Berryman, 1979). We design this example to test the capability of the scheme in dealing with both the vertical and lateral variations.

The grid sampling is $\Delta x_1 = \Delta x_3 = 0.01$ km and the maximum phase angle is taken as $\theta_{\max} = 80$ degrees; see Figure 2. Because of vertical and lateral variations of the example near the source, we can not use the initialization technique used in the first example; instead, we use horizontal qP sound speed $(= \alpha_0\sqrt{1+2\epsilon})$ and an adaptive integration method (Stoer and Bulirsch, 1992) to obtain the traveltime at $x_3 = 0$ km. Figure 2a shows the traveltime isochrons for the 2D model. Because the lateral variation is not symmetric with respect to the source, the isochrons could not reach the same depth at $x_1 = 0.5$ km and $x_1 = -0.5$ km, the isochron of 0.262 s, for example. Also, from the figure we can see that the limitation on the maximum phase angle (artificial plane wave approximation) plays a role when the phase angle is near 90 degrees. Figure 2b shows the calibration result for the traveltime at bottom $x_3 = 1.0$ km from the ENO scheme and the ray tracing method (Cerveny, 1972). Because the raytracing method can not give us the traveltime at grid point directly and we can not

guarantee that every traced ray will pass through the bottom, we have to use a linear interpolation method to extract the traveltime for some points (not necessarily grid points) from the ray tracing solutions. The ray tracing method uses the traveltime as a running parameter along the ray; i.e. (x_1, x_3, p_1, p_3) are parameterized by traveltime τ. When a ray passes through the bottom $x_3 = 1$ km, we pick out the nearest two points on the ray which embrace the bottom, then we approximate by linear interpolation the x_1 coordinate and the traveltime of the intersection point between the ray and the bottom. In the computation, the ray tracing method traces rays from phase angle -80 degrees to 80 degrees with a sampling interval of π degrees. Because the ray fan from ray tracing is rarefying quickly away from the source, most of the intersection points are not at the grid point, so it is not appropriate to assess the accuracy of the ENO scheme and ray tracing method this way. Nevertheless, they are perfectly consistent with each other; see Figure 2b. The effect of the lateral variations of the model is evident on the traveltime curves at the bottom.

3-D VTI

The 3-D VTI example is the homogeneous Green River shale, and the four Thomsen parameters are the same as in the 2D homogeneous case. The model occupies the cube $\{-0.5 \text{ km} \le x_1 \le 0.5 \text{ km}, -0.5 \text{ km} \le x_2 \le 0.5 \text{ km}, 0 \le x_3 \le 1.0 \text{ km} \}$, and the source is located at the center of the surface $x_3 = 0$.

The grid sampling is $\Delta x_1 = \Delta x_2 = \Delta x_3 = 0.02$ km, and the maximum phase angle is taken as $\theta_{\max} = 65$ degrees. We assume that the initial layer is homogeneous above 0.1 km, and we start the finite-difference scheme at 0.1 km. To initialize the traveltime at 0.1 km, we use the analytic method mentioned above. Figure 3a shows the isochrons at the bottom $x_3 = 1$ km, and the isochrons are circles because of the transverse isotropy. Figure 3b shows the vertical traveltime profile at $x_2 = 0.3$ km. Figure 4 shows the traveltime comparison at gridline $x_2 = 0.2$ km and $x_3 = 1.0$ km

between the ENO traveltime and the analytic traveltime, and the maximum absolute error is less than 0.19 ms.

Isotropic and VTI Marmousi model

Because the Marmousi model is well known as a complex velocity model, we test the ENO scheme to see its robustness and stability on the original isotropic and the anisotropic Marmousi model (Alkhalifah, 1997). We take portions of these two models to test our method; that is, the sampling domain is $\{4.5 \text{ km} \leq x_1 \leq 7.5 \text{ km}, 0 \leq x_3 \leq 2.9875 \text{ km} \}$, and the lateral and depth samples are 241 and 240, respectively, with the sampling intervals equal to 12.5 m.

In the computation, the maximum phase angle is taken as $\theta_{\max} = 75$ degrees. The source is located at $x_1 = 6.0$ km, $x_3 = 0.0$ km. For the isotropic Marmousi model, we initialize the traveltime at $x_3 = 0.0$ km by using the constant surface velocity. For the VTI Marmousi model, the traveltime is initialized by using the horizontal sound velocity. The final results are shown for windowed portions of the two models, corresponding to $\{5.4 \text{ km} \leq x_1 \leq 6.8 \text{ km}, 1.5 \text{ km} \leq x_3 \leq 2.9875 \text{ km} \}$; see Figure 5. Because the vertical velocity in the VTI Marmousi model is the same as the isotropic Marmousi model, the portion of the wavefront corresponding to vertical wave propagation is similar (Alkhalifah, 1997), which we can see by subtracting the two traveltime fields, with results shown in Figure 6. However, there are still some differences between the two models, especially near the upper-right corner where η is larger than other places, and the maximum traveltime difference is 5.9 ms. There are three possible reasons for these traveltime differences: the anisotropic effects, the upwind treatment of shocks in the numerical methods or the cutoff for phase angles $\geq \theta_{\max}$; which one responsible for the difference will be investigated elsewhere. These computations show that our scheme can deal with complex geological models.

CONCLUSIONS

We have formulated, for heterogeneous anisotropic solids, the paraxial eikonal equation satisfied by the first-arrival traveltime associated with the qP wave propagation. We have presented some implementation details for computing the paraxial Hamiltonian and illustrated the application to transversely isotropic solids; for complete implementation details, see Qian (2000). We have constructed a second-order scheme by using a first-order scheme (Qian, 2000) as a building block. Higher order schemes may be constructed by further use of this method (Qian et al., 1999). These schemes solve the qP paraxial eikonal equation in $O(N)$ floating point operations (where N is the number of grid points). Extensive numerical results have shown that our scheme is accurate, efficient and can deal with complex models and models with both lateral and vertical variations. The chief shortcoming is that the paraxial assumption permits us to compute traveltimes along downgoing rays only; for example, we do not compute the overturning wavefronts, therefore the velocity structure is limited to be of mild lateral heterogeneity.

The scheme can be used in many geophysical applications requiring modeling anisotropic wave propagation such as 3-D Kirchhoff migration and modeling, tomography, and 3-D controlled illumination modeling.

ACKNOWLEDGEMENTS

The authors performed part of the research reported here while guests of the Stanford Exploration Project; J. Qian and W.W. Symes thank SEP members and director Prof. Jon Claerbout, for their hospitality and many stimulating discussions. J. Qian thanks Dr. Joe Dellinger, Dr. S. Kim and Prof. B. Cockburn for a lot of helpful discussion and encouragement. The authors also would like to thank the associate editor, Kurt Marfurt, and anonymous referees for beneficial comments.

This work was partially supported by the National Science Foundation under grant numbers DMS 9627355, the Office of Naval Research under grant number N00014-96-1-0156, the U. S. Department of Energy under grant number DE-FG07-97 ER14827 and The Rice Inversion Project. TRIP Sponsors for 1999 are Amerada Hess, Amoco Research, Conoco Inc., Exxon Production Research Co., Geophysical Development Corporation, Landmark Graphics, Mobil, and Western Geophysical.

REFERENCES

Alkhalifah, T., 1997, Anisotropic Marmousi data set: SEP95.

Anderson, J. E., 1996, Imaging in transversely isotropic media with a vertical symmetry axis: Ph.D. thesis, Center for Wave Phenomena, Colorado School of Mines, Golden, CO80401-1887.

Berryman, J. G., 1979, Long-wave elastic anisotropy in transversely isotropic media: Geophysics, **44**, 896–917.

Cerveny, V., 1972, Seismic rays and ray intensities in inhomogeneous anisotropic media: Geophys. J. Roy. Astr. Soc., **29**, 1–13.

Cherrett, A., and Singh, S., 1998, Traveltime and polarisation tomography in 3-D anisotropic media: 68th Ann. Internat. Mtg., Soc. Expl. Geophys., Expanded Abstracts, 1859–1862.

Crandall, M. G., and Lions, P. L., 1983, Viscosity solutions of Hamilton-Jacobi equations: Trans. Am. Math. Soc., **277**, 1–42.

Crandall, M. G., Ishii, H., and Lions, P. L., 1992, User's guide to viscosity solutions of second order partial differential equations: Bull., Am. Math. Soc., **27**, 1–67.

Dellinger, J., and Symes, W. W., 1997, Anisotropic finite-difference traveltimes using a Hamilton-Jacobi solver: 67th Ann. Internat. Mtg., Soc. Expl. Geophys., Expanded Abstracts, 1786–1789.

Dellinger, J., 1991, Anisotropic seismic wave propagation: Ph.D. thesis, Stanford University, Stanford, CA94305.

El-Mageed, M. A., Kim, S., and Symes, W. W., 1997, 3-D Kirchhoff migration using finite difference traveltimes and amplitudes: Annual Report. The Rice Inversion Project (http://www.trip.caam.rice.edu/).

Fedorov, F. I., 1968, Theory of elastic waves in crystals: Plenum press.

Gray, S., and May, W., 1994, Kirchhoff migration using eikonal equation traveltimes: Geophysics, **59**, 810–817.

Kim, S., and Cook, R., 1999, 3-D traveltime computation using second-order ENO scheme: Geophysics, **64**, 1867–1876.

Lions, P. L., 1982, Generalized solutions of Hamilton-Jacobi equations: Pitman Advanced Publishing Program.

Meng, Z., and Bleistein, N., 1997, Wavefront construction ray tracing in tetrahedral models: CWP-251, Center for Wave Phenomena, Colorado School of Mines.

Musgrave, M. J. P., 1970, Crystal acoustics: Holden-Day.

Osher, S. J., and Sethian, J. A., 1988, Fronts propagating with curvature dependent speed: algorithms based on Hamilton-Jacobi formulations: J. Comput. Phys., **79**, 12–49.

Osher, S. J., and Shu, C. W., 1991, High-order Essentially NonOscillatory schemes for Hamilton-Jacobi equations: SIAM J. Num. Anal., **28**, 907–922.

Pratt, R., and Chapman, C., 1992, Traveltime tomography in anisotropic media -II: Application: Geophys. J. Internat., **109**, 20–37.

Qian, J., Belfi, C. D., and Symes, W. W., 1999, Adaptive finite difference method for traveltime and amplitude: 69th Ann. Internat. Mtg., Soc. Expl. Geophys., Expanded Abstracts, 1763–1766.

Qian, J., 2000, Geometrical optics for Quasi-P waves: Theories and numerical methods: Ph.D. thesis, Rice University, Houston, TX77251-1892.

Qin, F., and Schuster, G. T., 1993, First-arrival traveltime calculation for anisotropic media: Geophysics, **58**, 1349–1358.

Reshef, M., and Kosloff, D., 1986, Migration of common shot gathers: Geophysics, **51**, 324–331.

Schneider, W. A. J., Ranzinger, K., Balch, A., and Kruse, C., 1992, A dynamic programming approach to first arrival traveltime computation in media with arbitrarily distributed velocities: Geophysics, **57**, 39–50.

Schneider, W. A. J., 1995, Robust and efficient upwind finite-difference traveltime calculations in three dimensions: Geophysics, **60**, 1108–1117.

Sethian, J. A., and Popovici, A. M., 1999, 3-D traveltime computation using the fast marching method: Geophysics, **64**, 516–523.

Shearer, P. M., and Chapman, C. H., 1988, Ray tracing in anisotropic media with a linear gradient: Geophysical Journal, **94**, 575–580.

Shu, C. W., 1998, Essentially non-oscillatory and weighted essentially non-oscillatory schemes for hyperbolic conservation laws *in* Cockburn, B., Johnson, C., Shu, C., and Tadmor, E., Eds., Advanced Numerical Approximation of Nonlinear Hyperbolic Equations:: Lecture Notes in Mathematics, volume 1697, Springer, 325–432.

Stoer, J., and Bulirsch, R., 1992, Introduction to numerical analysis: Springer-Verlag, New York, second edition.

Symes, W. W., Versteeg, R., Sei, A., and Tran, Q. H., 1994, Kirchhoff simulation, migration and inversion using finite difference traveltimes and amplitudes: Annual Report, The Rice Inversion Project, (http://www.trip.caam.rice.edu/).

Thomsen, L., 1986, Weak elastic anisotropy: Geophysics, **51**, 1954–1966.

Tsvankin, I., and Thomsen, L., 1995, Inversion of reflection traveltimes for transverse isotropy: Geophysics, **60**, 1095–1107.

van Trier, J., and Symes, W. W., 1991, Upwind finite-difference calculation of traveltimes: Geophysics, **56**, 812–821.

Vidale, J., 1988, Finite-difference calculation of travel times: Bull., Seis. Soc. Am., **78**, 2062–2076.

TABLES

TABLE 1. Convergence order of the scheme (see text for explanation)

Δx_1	Abs.Err$(\tau, \Delta x_1)$(s)	Rel.Err$(\tau, \Delta x_1)$	α
0.08	7.3754e-04	0.00168	
0.04	2.1380e-04	6.1296e-04	1.45
0.02	5.5932e-05	1.6035e-04	1.93
0.01	1.4162e-05	4.0602e-05	1.98
0.005	3.5643e-06	1.0218e-05	1.99

FIGURES

FIG. 1. The p_3 components of outward normals at the two intersections on the convex slowness surface have opposite signs.

FIG. 2. (a) Traveltime isochrons for the 2-D model with vertical and lateral variations: effects of anisotropy and lateral heterogeneity on the wave propagation are evident. (b) Traveltime comparison at $x_3 = 1.0$ km for the model with vertical and lateral variations: ENO traveltime (*) and Ray-tracing traveltime (-) are consistent with each other.

FIG. 3. 3-D homogeneous VTI model. The source is located at $x_1 = x_2 = x_3 = 0.0$. (a) Horizontal traveltime slice at $x_3 = 1.0$ km: isochrons are circles because of the transverse isotropy. (b) Vertical traveltime slice at $x_2 = 0.30$ km.

FIG. 4. Traveltime comparison at gridline $x_2 = 0.2$ km, $x_3 = 1.0$ km for 3-D homogeneous VTI model: ENO traveltime (*) and Analytic traveltime (-); ENO traveltime has almost the same accuracy as the analytic traveltime.

FIG. 5. Traveltime contours overlaying the model. The source is positioned at $x_1 = 6.0$ km, $x_3 = 0.0$ km. (a) Isotropic Marmousi velocity model. (b) Anisotropic Marmousi η model.

FIG. 6. Anisotropic effects on the wave propagation. (a) Nonzero contours of traveltime differences between the two Marmousi models concentrate on the region where η is larger. (b) Contours of traveltime differences overlaying η model; the maximum traveltime difference is 5.9ms. See text for explanation of these differences.

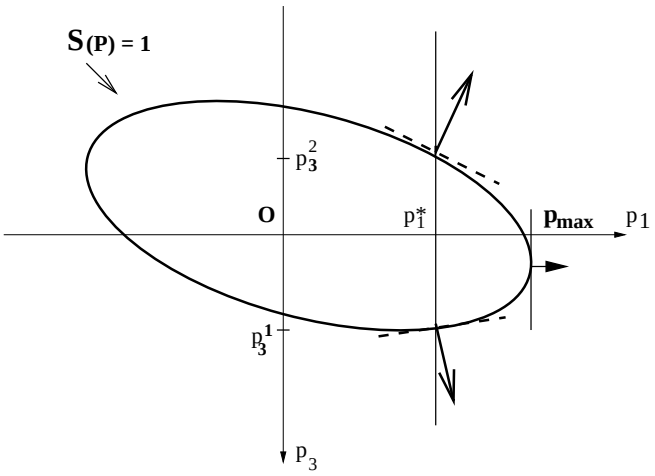

FIG. 1. The p_3 components of outward normals at the two intersections on the convex slowness surface have opposite signs.

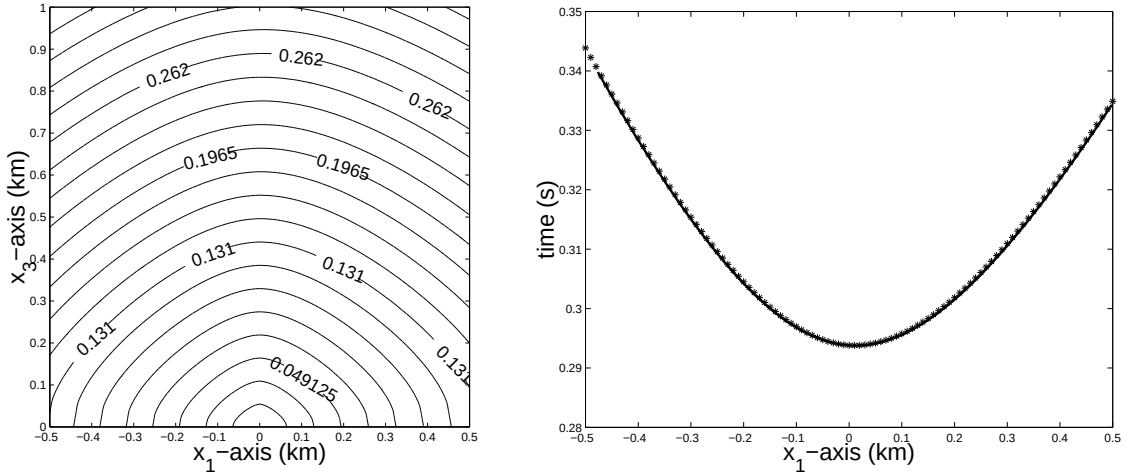

FIG. 2. (a) Traveltime isochrons for the 2-D model with vertical and lateral variations: effects of anisotropy and lateral heterogeneity on the wave propagation are evident. (b) Traveltime comparison at $x_3 = 1.0$ km for the model with vertical and lateral variations: ENO traveltime (*) and Ray-tracing traveltime (-) are consistent with each other.

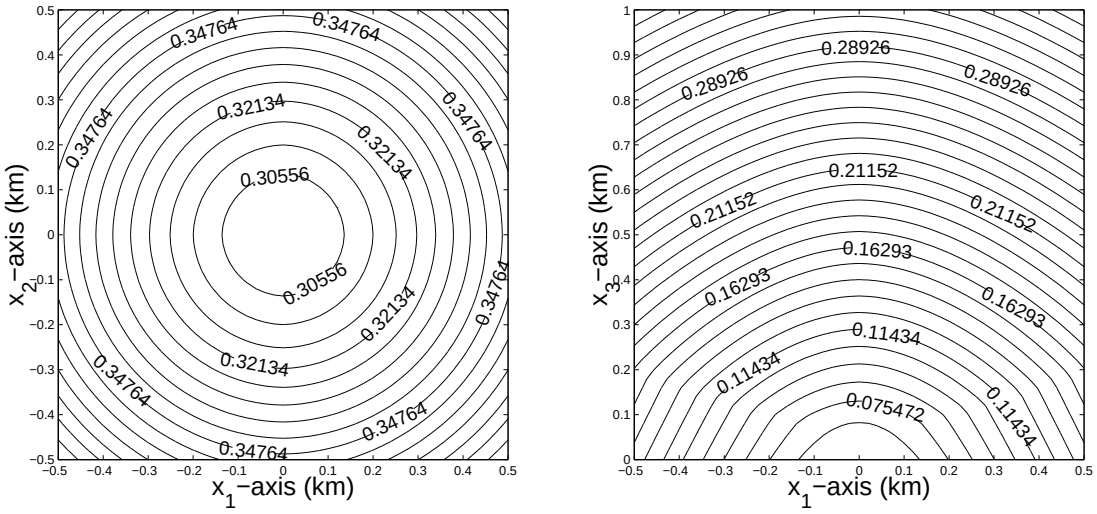

FIG. 3. 3-D homogeneous VTI model. The source is located at $x_1 = x_2 = x_3 = 0.0$. (a) Horizontal traveltime slice at $x_3 = 1.0$ km: isochrons are circles because of the transverse isotropy. (b) Vertical traveltime slice at $x_2 = 0.30$ km.

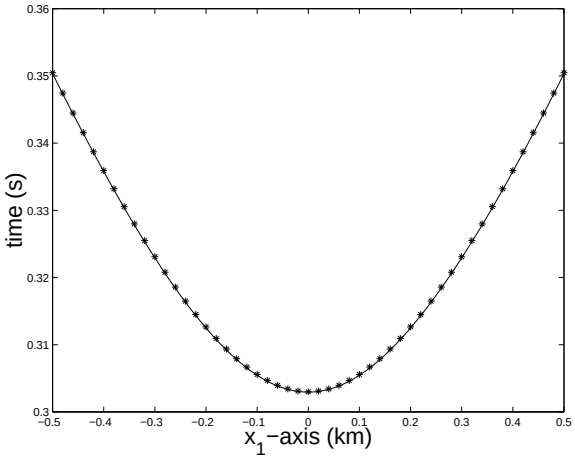

FIG. 4. Traveltime comparison at gridline $x_2 = 0.2$ km, $x_3 = 1.0$ km for 3-D homogeneous VTI model: ENO traveltime (*) and Analytic traveltime (-); ENO traveltime has almost the same accuracy as the analytic traveltime.

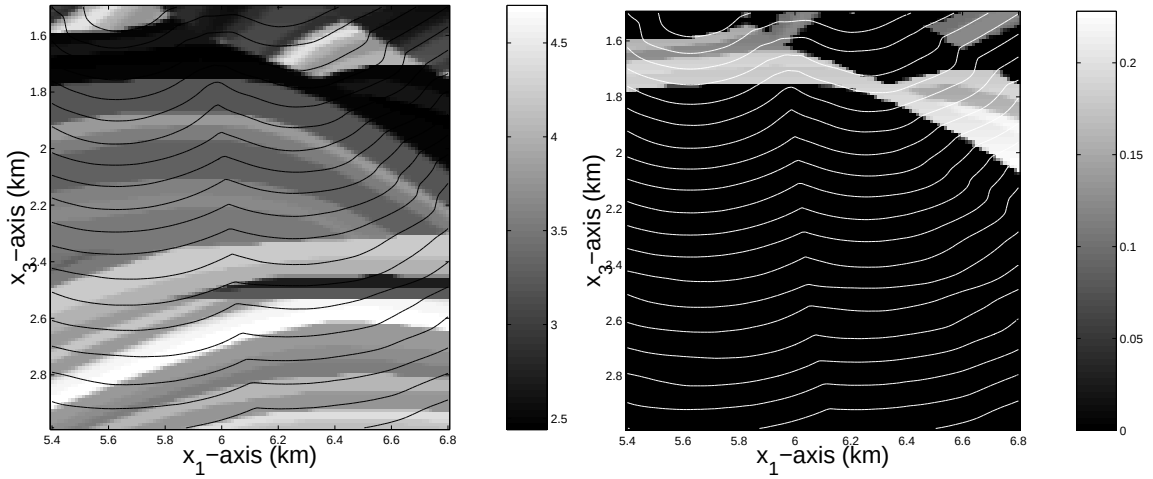

FIG. 5. Traveltime contours overlaying the model. The source is positioned at $x_1 = 6.0$ km, $x_3 = 0.0$ km. (a) Isotropic Marmousi velocity model. (b) Anisotropic Marmousi η model.

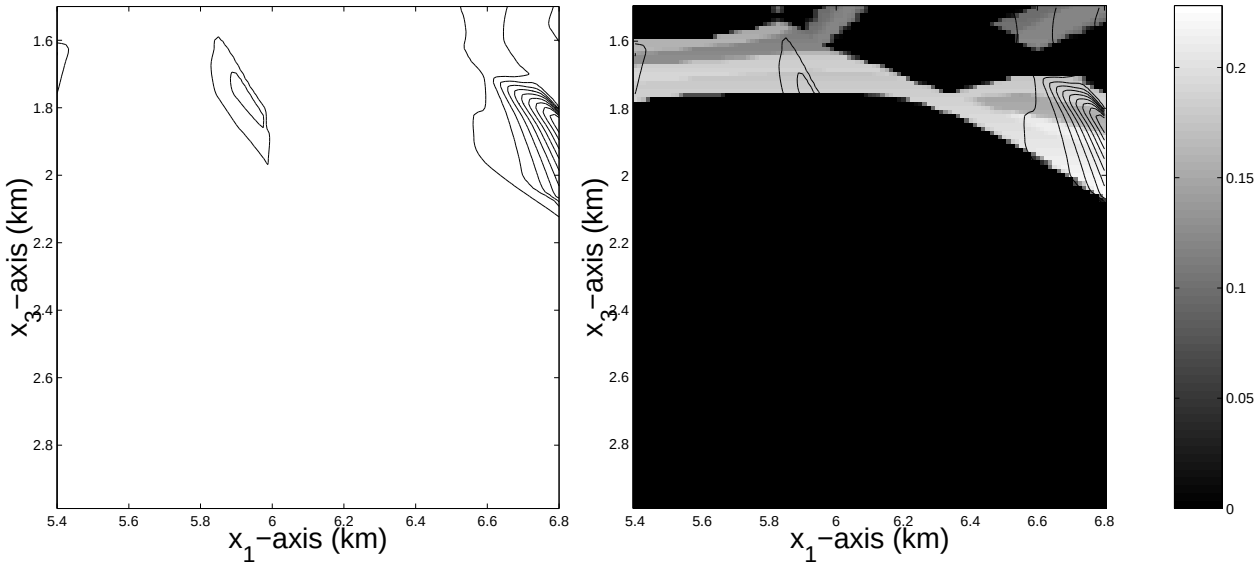

FIG. 6. Anisotropic effects on the wave propagation. (a) Nonzero contours of traveltime differences between the two Marmousi models concentrate on the region where η is larger. (b) Contours of traveltime differences overlaying η model; the maximum traveltime difference is 5.9ms. See text for explanation of these differences.